Dielectric capping effects on binary and ternary topological insulator surface states

Jiwon Chang,* Priyamvada Jadaun, Leonard F. Register, Sanjay K. Banerjee, and Bhagawan Sahu
Microelectronics Research Center, The University of Texas at Austin, Austin, Texas 78758, USA
(Received 10 December 2010; revised manuscript received 2 August 2011; published 10 October 2011)

Using a density-functional-based electronic structure method, we study the effect of crystalline dielectrics on the metallic surface states of Bismuth- and chalcogen-based binary and ternary three-dimensional topological insulator (TI) thin films. Crystalline quartz (SiO_2) and boron nitride (BN) dielectrics were considered. Crystalline approximation to the amorphous quartz allows one to study the effect of oxygen coverage or environmental effects on the surface-state degradation, which has gained attention recently in the experimental community. We considered both *symmetric* and *asymmetric* dielectric cappings to the surfaces of TI thin films. Our studies suggest that BN and quartz cappings have negligible effects on the Dirac cone surface states of both binary and ternary TIs, except in the case of an oxygen-terminated quartz surface. Dangling bond states of oxygens in oxygen-terminated quartz dominate the region close to Fermi level, thereby distorting the TI Dirac cone feature and burying the Dirac point in the quartz valence-band region. Passivating the oxygen-terminated surface with atomic hydrogen removes these dangling bond states from the Fermi-surface region, and consequently the clear Dirac cone is recovered. Our results are consistent with recent experimental studies of TI surface degradation in the presence of oxygen coverage.

DOI: 10.1103/PhysRevB.84.155105 PACS number(s): 71.15.Dx, 71.18.+y, 73.20.At, 73.61.Le

I. INTRODUCTION

Three-dimensional (3D) topological band insulator (TI) Bi_2X_3 (X = Se, Te) and its ternary counterparts have attracted considerable attention from the condensed-matter physics community because of the relatively simple crystal structure that hosts novel surface states,[1,2] and their unusual responses to external fields. Many more 3D TI materials have been predicted[3–7] by now, and the quest for studying their novel surface-state properties, in isolation as well as in the presence of other materials, has increased in recent years. The 3D TI surface states are time-reversal symmetric (TRS) at high-symmetry points in the momentum space and are therefore protected against perturbations which cannot break TRS such as nonmagnetic impurities or adatoms. Such novel properties have caused excitement in the electron device community as well because it can be a potential alternative to graphene as a channel material in field-effect transistors. The advances in understanding of structural, electronic, magnetic, and transport properties of 3D TI, made possible by both experimental and theoretical studies,[8–10] can provide important information for novel applications. Besides the fundamental studies of these model 3D TI materials, theoretically, no studies of dielectric effects on the surface states have been performed so far from first principles. We address dielectric effects on the TI surface states using *ab initio* density functional theory (DFT) and semilocal density approximation.[11] Two crystalline dielectrics were considered: quartz (SiO_2) and boron nitride (BN). Both binary TI Bi_2Se_3 and ternary TIs Bi_2Se_2Te and Bi_2Te_2Se were considered for this study. Our studies suggest that neither of the two dielectrics has an effect on the Dirac cone except the oxygen-terminated quartz. Under the environment of oxygen dangling bonds, the Dirac cone on the TI surface is buried inside the quartz valence-band continuum with the oxygen dangling-bond states occupying the region around the Fermi level. Surface passivation by atomic hydrogen pushes the dangling-bond states from the Fermi-surface region down below Fermi level and a clear Dirac cone emerges at the Fermi level. These findings are consistent with recent experimental studies of surface degradation effects in the presence of oxygen.[14]

We begin by describing the thin-film structures of both binary and ternary TIs, built from their bulk hexagonal structures, and the computational method in Sec. II. In Sec. III, we present the dielectric capping effects, by BN and SiO_2, on metallic surface states of TIs. Both *symmetric* and *asymmetric* cappings are explored. Finally we present our summary and conclusions.

II. ISOLATED THIN FILMS AND COMPUTATIONAL APPROACH

The thin-film structures for both binary and ternary TIs are constructed by stacking up several quintuple layers (or QLs: 1 QL = 5 atomic layers) along the crystallographic z direction with a vacuum region of 3 nm, which forms the supercell in the DFT calculation. The first-principle calculations were performed using the OPENMX code,[15] based on a linear combination of the pseudoatomic orbital (PAO) method.[16] The pseudopotentials were generated from full relativistic calculations, and the generalized gradient approximation[11] was applied for the exchange-correlation potential. The kinetic energy cutoff of 180 Ry and the **k**-point mesh of $7 \times 7 \times 1$ for Brillouin zone (BZ) integration [Fig. 1(c)] were used. The basis sets were carefully chosen to reproduce previous bulk and thin-film calculations. The cutoff, **k**-point mesh, and vacuum region were optimized to guarantee the convergence of the results and their agreement with previous theoretical calculations.

For the binary TI, previous theoretical studies of bulk Bi_2Se_3 found the computed lattice parameters close to the experimental values,[8] so we used the experimental lattice parameters $a = 0.41388$ nm and $c = 2.8633$ nm in the hexagonal unit cell and optimized bulk atomic positions to build the thin-film structure. For the ternary TI Bi_2Se_2Te (Bi_2Te_2Se), we built thin-film structures with the bulk hexagonal

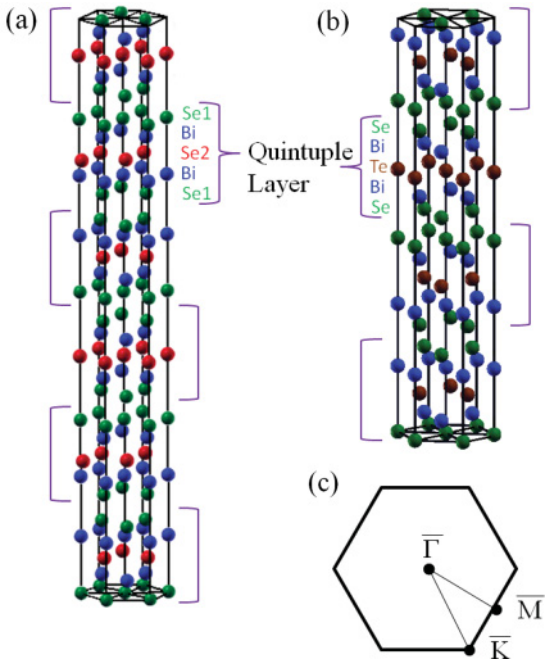

FIG. 1. (Color online) Schematic diagram of (a) 6 QLs Bi_2Se_3 and (b) 4 QLs Bi_2Se_2Te thin-film structures obtained by stacking QLs along the z direction. (c) Two-dimensional Brillouin zone (BZ) of the (111) surface of thin-film TIs with three time-reversal invariant points $\bar{\Gamma}$, $\bar{M}$, and $\bar{K}$.

unit-cell lattice parameters $a = 0.422$ nm (0.428 nm) and $c = 2.92$ nm (2.99 nm) in the previous theoretical calculation,[19] and optimized the thin-film structure by letting atoms move along the z direction. We optimized thin-film structures only for ternary TIs, since atomic relaxations significantly affect the band structure of thin-film Bi_2Se_2Te around the Dirac point.[19] We considered the thin film of 6 QLs and 4 QLs for binary and ternary TIs, respectively, since previous studies on binary[17,18] and ternary[19] TIs suggest that 6 QLs and 4 QLs are the minimum thicknesses to maintain the gapless surface state at the Dirac point. We also obtained the same critical thickness values by our own calculations. In the calculated band structure of 6 QLs Bi_2Se_3, we could observe the Dirac cone within a bulk gap of 0.262 eV. For the ternary TIs Bi_2Se_2Te and Bi_2Te_2Se, Dirac cone surface states reside inside the bulk gap of 0.204 and 0.325 eV, respectively.

III. THIN FILMS WITH SYMMETRIC AND ASYMMETRIC DIELECTRIC CAPPINGS

We chose crystalline SiO_2 in order to assess the effect of oxygen environment on the TI surface states. The choice of BN dielectrics is perhaps guided by the recent graphene transport experiments using crystalline dielectrics.[12,13] We considered both symmetric and asymmetric cappings in terms of relative orientations of TI and dielectric surface atoms. Asymmetry in terms of different dielectrics on two opposite TI surfaces was not considered.

The bulk structures of both dielectrics were studied with the computational parameters described in the previous section. For the hexagonal BN, the experimental lattice paramters are $a = 0.2494$ nm and $c = 0.666$ nm with the distance between B and N $d_{B\text{-}N} = 0.144$ nm,[20] and the band gap is 5.97 eV.[21] We used the experimental values of lattice constants and atomic positions. With these experimental values, our calculated bulk band-gap value is 5.5 eV, close to the experimental value 5.97 eV. The hexagonal crystal structure of quartz contains fourfold coordinated oxygens, forming a layered structure with Si, with the experimental lattice parameters ($a = 0.4914$ nm and $c = 0.5408$ nm,[22]). Our DFT calculations of optimized lattice parameters with semilocal potentials are found to be close to these experimental values, accurate to within 0.1%. Therefore, we chose experimental lattice parameters for building our interface structures of TI and quartz. The bulk quartz SiO_2 has a direct band gap of 9 eV,[23] and our DFT calculation of crystalline SiO_2 results in a band-gap value of 9.4 eV. We note that our results obtained for quartz should be considered, at best, qualitative with regard to TIs capped with amorphous SiO_2.

A. Thin films of binary TI Bi_2Se_3 with dielectrics

In this section, we discuss the thin film of binary TI Bi_2Se_3.

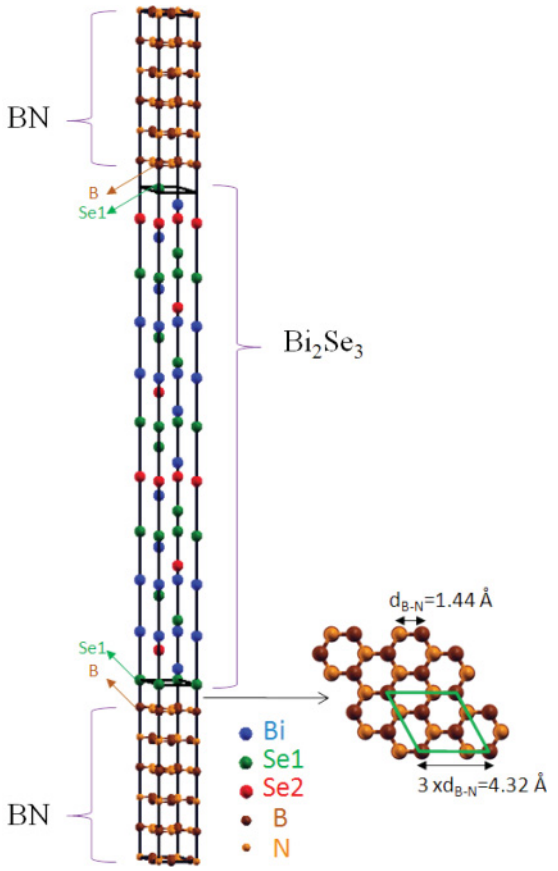

FIG. 2. (Color online) Schematic diagram of the supercell structure of BN and 6 QLs Bi_2Se_3. The colors corresponding to the atoms are labeled on the bottom right of the supercell. The green and brown arrows at the top and bottom interfaces indicate B on the top of Se. The top view of bottom interfacial atomic layers is shown on the bottom right of the supercell structure. The 1×1 Bi_2Se_3 cell (green rhombus) is matched with $3d_{B\text{-}N} \times 3d_{B\text{-}N}$ BN. This corresponds to symmetric capping mentioned in the text. Also, Se on the top of N on both sides of the film corresponds to the symmetric case.

1. Construction of supercell structure

The interface structures are built by putting the dielectric material on the surfaces of 6 QLs of Bi_2Se_3 film stacked along the z direction (since it has no band gap for the surface states). In constructing supercells, we maintained the TI lattice and strained the dielectrics to fit with the TI surface resulting in the compressive or tensile strain on the dielectrics to focus on their effects on the TI electronic structure. For the BN, our analysis suggests that to keep our computational burden in DFT-based calculations minimal, $3d_{\text{B-N}} \times 3d_{\text{B-N}}$ lattice structure can be matched in-plane with a 1×1 Bi_2Se_3 cell (Figs. 2 and 3) or any multiples of this combination which maintain a 3:1 matching ratio resulting in the 4.19% compressive strain on BN (in Table I). Other combinations to allow less strain result in either difficulty in forming the periodic structure or larger supercells with orders of magnitude more atoms. Along the stacking direction, 6 QLs of Bi_2Se_3 (∼6 nm) is put on six atomic layers of BN (∼1.7 nm). The choice of six BN layers is somewhat arbitrary and guided by the fact that the size of vacuum and BN layers should be thick enough to avoid interactions of periodically repeated Bi_2Se_3 surface layers. We also relaxed the interfacial atoms to assess its effects. For the SiO_2 dielectric, the supercell structure consists of two unit cells of SiO_2 sandwiching 6 QLs Bi_2Se_3. The size of SiO_2 and Bi_2Se_3 cells along the x-y direction chosen is, respectively, 1×1 and 2×2 (Fig. 4) to minimize the computational cost. This produces about 2.75% compressive strain on both sides of SiO_2, as in Table I. Consideration of larger sizes can lead to the lower strain, but the total number of atoms in the cell increases at least an order of magnitude (250 versus 2500).

TABLE I. Hexagonal unit-cell lattice constant a of binary TI and strains on dielectrics by the lattice mismatch at the interface.

TI	a (nm)	Strain on SiO_2	Strain on BN
Bi_2Se_3	0.41388	2.75% compressive	4.19% compressive

We considered four configurations of Se positions on the TI surfaces with respect to boron and nitrogen positions on the BN layer: Se on the top of B, on the top of N, on the

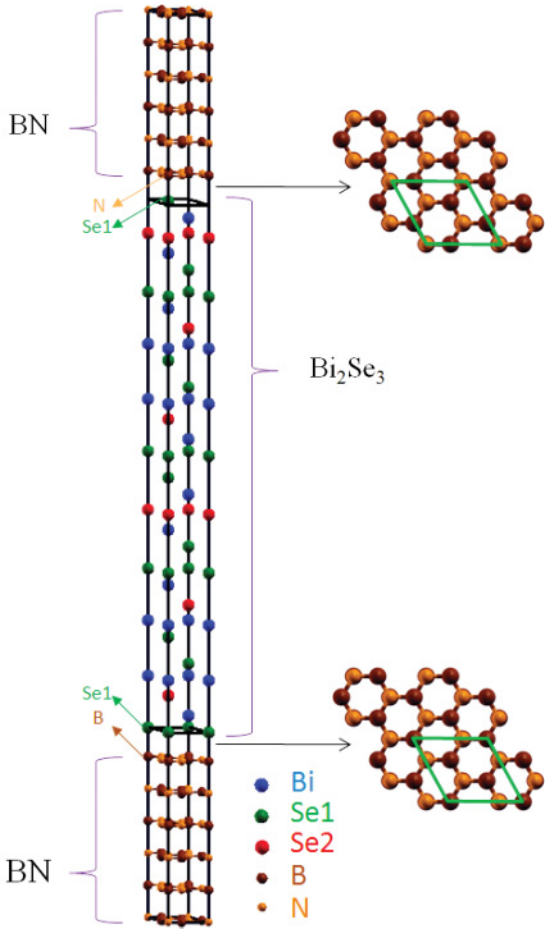

FIG. 3. (Color online) Same as Fig. 2 but now with the B on the top of Se on one side and N on the top of Se on the other side of the TI thin film. The colors corresponding to atoms are labeled on the bottom right of the supercell. The green, brown, and orange arrows indicate the relative positions of the Se atom with respect to B (bottom) and N (top). The top views of top and bottom interfacial atomic layers are shown on the top right and bottom right of the supercell, respectively. The 1×1 Bi_2Se_3 cell (green rhombus) is matched with $3d_{\text{B-N}} \times 3d_{\text{B-N}}$ BN. This corresponds to asymmetric capping in the text.

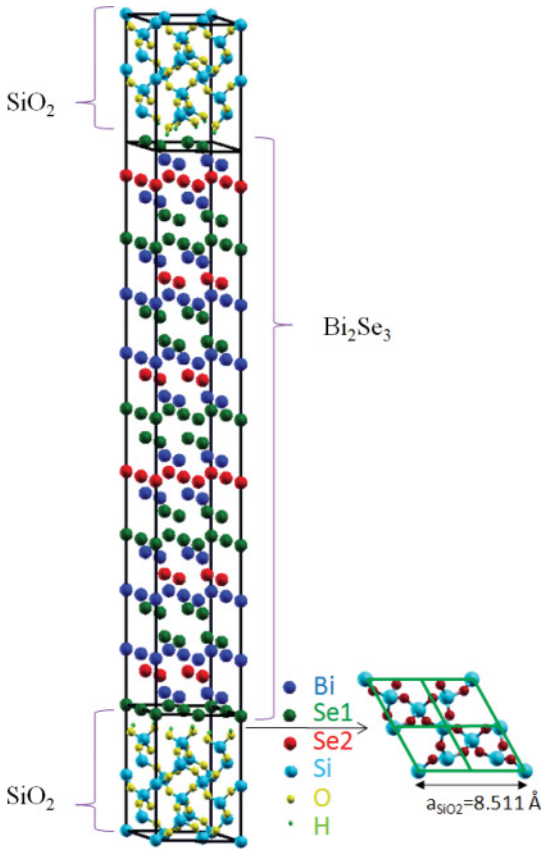

FIG. 4. (Color online) Schematic diagram of oxygen-terminated quartz with dangling-bond states covered with hydrogen atoms (small green circles) interfaced on both sides of Bi_2Se_3. The Si-terminated surface also possesses dangling bonds, but only oxygen-terminated surface without the hydrogen coverage distorts the surface-state Dirac cone. The top view of bottom interfacial atomic layers is shown on the bottom right of the supercell structure. The 2×2 Bi_2Se_3 cell (green rhombus) is matched with 1×1 SiO_2 at the interface.

hexagonal hole, and on the bond between B and N atoms. Two surface terminations, Si and oxygen, of quartz were considered. Our calculations suggest that all BN configurations are energetically close and provide quite similar band structures. Therefore, we had a choice in the selection of a particular configuration for further studies. We chose the case of B or N on the top of Se on both TI surfaces. We refer to the structure of B or N on the top of Se on both sides of TI film as *symmetric* capping (Fig. 2). The structures of B on the top of Se on one side and N on the top of Se on the other side of TI film, or only B or N on one side of TI film and vacuum on the other side, are referred to as *asymmetric* capping (Fig. 3). For quartz, both TI surfaces capped with either oxygen-terminated or Si-terminated quartz were considered. Because quartz is a fourfold coordinated structure, both of the surface terminations of quartz possess dangling bonds. Therefore, for quartz we also considered the dangling-bond saturation with hydrogen; that is, hydrogen passivation of the quartz surfaces.

To set the optimal distance between the BN and Bi_2Se_3 layers at the interface, we performed the total energy calculations at the chosen set of interfacial distances. Our studies suggest an optimal distance of 0.3 nm for the case of the Se layer in Bi_2Se_3 on the top of either B or N in BN. For Bi_2Se_3 on quartz, the interfacial distances for Si and oxygen quartz terminations with and without hydrogen passivation need to be considered. Our studies suggest an optimal distance of 0.3 nm for Si-terminated surface, regardless of whether dangling bonds are saturated or not. For the oxygen-terminated quartz with hydrogen passivation, we found the optimal distance to

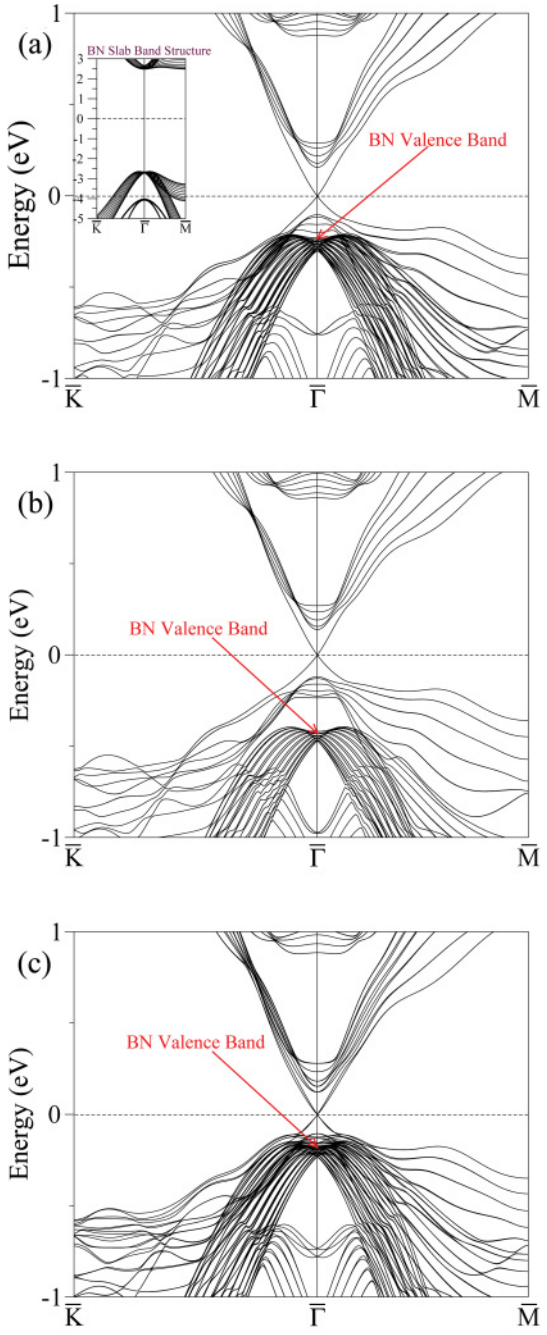

FIG. 5. (Color online) Band structures of Bi_2Se_3/BN supercell along high-symmetry directions of the hexagonal BZ for symmetric capping case (a) B on the top of Se and (b) N on the top of Se on both sides of TI film without atomic relaxation. The Dirac cone and its degeneracy at the $\bar{\Gamma}$ point are not disturbed in the presence of crystalline BN thin film. (c) Same case of (a) with atomic relaxation. Atomic relaxation has little effect on the Dirac cone feature. The position of BN valence-band maximum can be found by the band structure of a BN slab without TI in the inset of (a) and the density of states (DOS) plots in Fig. 6.

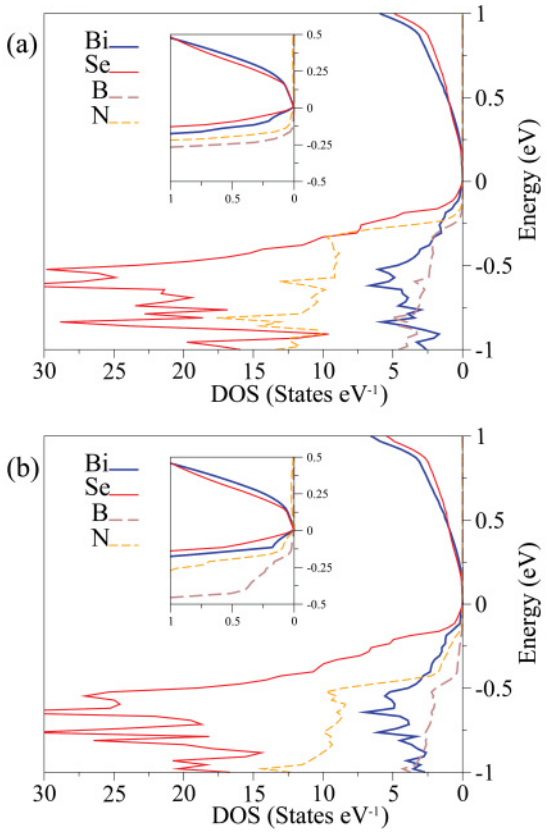

FIG. 6. (Color online) The atom-projected DOS in the same energy range as the band structures in Fig. 5 for symmetric capping cases (a) B on the top of Se and (b) N on the top of Se on both sides of TI film without atomic relaxation. Se orbitals are not in *resonance*, with either B or N orbitals near the Fermi level suggesting that the Dirac cone, formed from the Bi and Se orbitals, is intact.

be 0.25 nm. We considered these optimal interfacial distances in our further studies.

We considered the atomic relaxation in the interfacial region in order to check its effect on the electronic structure of TI surface states. Two cases were considered: first is the case of Se on the top of the B atom on both sides of TI with the initial optimal separation of 0.3 nm. We let atoms close to the interface (Bi/Se atoms in the top and bottom QLs and B/N atoms in the two layers next to TI surfaces) move in the z direction. The second choice is that the oxygen-terminated quartz with the saturation of dangling bonds is put on both TI surfaces with optimal separation of 0.25 nm. Bi/Se atoms in the top and bottom QLs as well as Si/O atoms next to the TI surfaces are allowed to move in the z direction, while hydrogen atoms used to saturate dangling bonds are relaxed in all directions.

2. *Results and discussion*

We first discuss the BN interface effects followed by the effects due to quartz surface terminations. Figures 5(a) and 5(b), respectively, show the band structures of 6 QLs Bi_2Se_3 capped on both sides by BN with either B on the top of the Se atom or N on the top of the Se atom (symmetric capping). The atomic relaxation is not considered here. The Dirac cone and its degeneracy are protected in both cases. This insensitivity of the Dirac cone to the presence of dielectric hints at negligible interactions between B or N orbitals with Se orbitals. We confirm this hypothesis by plotting atom-projected DOS in the same energy range as the band structures in Figs. 6(a) and 6(b). These plots show that both B and N orbitals are not in *resonance* with the Se orbitals of TI. As a result, the Dirac cone surface states are protected. From the band structure of only BN atomic layers without Bi_2Se_3 [inset in Fig. 5(a)] and the atom-projected DOS plots of Figs. 6(a) and 6(b), the BN valence-band maximum is estimated to be about 0.25 and 0.45 eV below the Dirac point for B on the top of Se atom and N on the top of Se atom cases, respectively. The band structure including the effect of atomic relaxation for the structure of B on the top of Se on both sides is shown in Fig. 5(c). A comparison of Fig. 5(c) with Fig. 5(a) indicates that the relaxation of interfacial atomic positions does not affect the essential characteristics of surface states

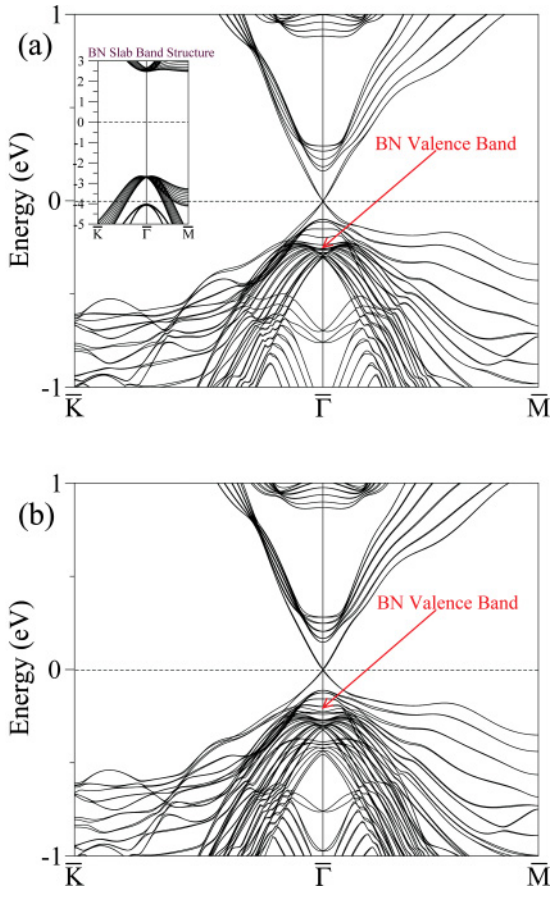

FIG. 7. (Color online) Band structures of Bi_2Se_3/BN supercell along high-symmetry directions of the hexagonal BZ for asymmetric capping cases (a) B on the top of Se on one side and vacuum on the other side of TI film and (b) B on the top of the Se atom on one side and N on the top of the Se atom on the other side without atomic relaxation. The Dirac cone and its degeneracy at the $\bar{\Gamma}$ point are not disturbed in the presence of crystalline BN thin film. The position of BN valence-band maximum can be found by the band structure of the BN slab without TI in the inset of (a) and the DOS plots in Fig. 8.

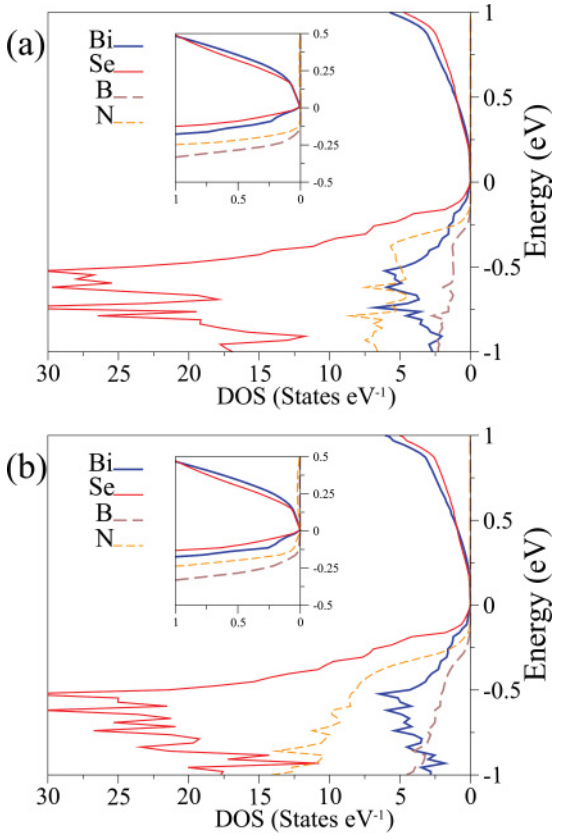

FIG. 8. (Color online) The atom-projected DOS in the same energy range as the band structures in Fig. 7 for asymmetric capping cases (a) B on the top of Se on one side and vacuum on the other side of TI film and (b) B on the top of Se on one side and N on the top of Se on the other side of TI film without relaxation. Se orbitals are not in resonance, with either B or N orbitals near the Fermi level suggesting that Dirac cone, formed from the Bi and Se orbitals, is intact.

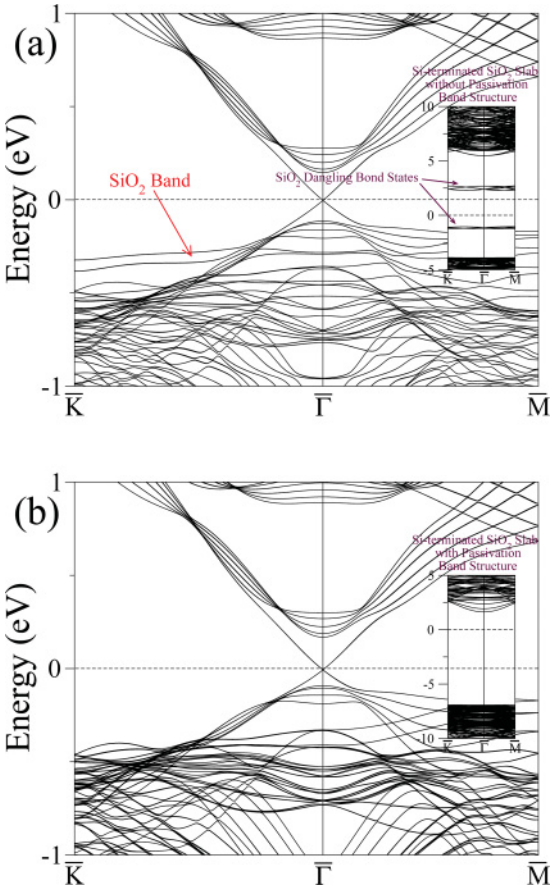

FIG. 9. (Color online) Band structure of Bi_2Se_3 with Si-terminated quartz supercell along high-symmetry directions in the hexagonal BZ (a) without hydrogen coverage and (b) with hydrogen coverage. The Dirac cone of TI is preserved in both cases. Insets of (a) and (b) show the band structures of only Si-terminated SiO_2 slabs without and with passivation, respectively. In the inset of (b), a clear band gap is seen, while additional bands by Si dangling bond lie inside the gap in the inset of (a).

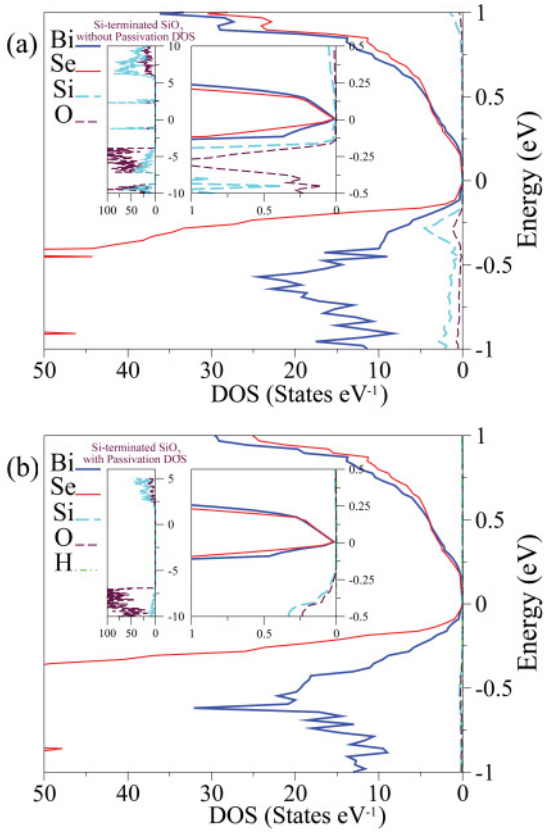

FIG. 10. (Color online) The atom-projected DOS in the same energy range as the band structures in Fig. 9 for the Si-terminated quartz cases (a) without hydrogen passivation and (b) with hydrogen passivation. The orbitals of Si and Se do not overlap near the Fermi level. Left insets of (a) and (b) show the atom-projected DOS for only Si-terminated SiO_2 slabs without and with passivation, respectively. States from Si orbitals are clearly shown in the left inset of (a).

near the Fermi surface. Fourfold degeneracy at the Dirac point and the dispersion relation still remain the same, while valence bands of BN are shifted a bit closer to the Dirac point. The bulk band-gap size for each case (0.259 eV for B on the top of Se, 0.258 eV for N on the top of Se) does not change much from that of only 6 QLs Bi_2Se_3 (0.262 eV).

In the case of asymmetric capping, B on the top of the Se atom on one side and vacuum on the other side of the TI film shows that the Dirac point degeneracy is still unaffected in Fig. 7(a). However, there is some splitting of valence and conduction bands close to it. With B on the top of Se on one side and N on the top of Se on the other side, the Dirac cone is not influenced either, as seen in Fig. 7(b). Again, the atom-projected DOS plots in Figs. 8(a) and 8(b) suggest that this insensitivity is due to nonoverlap of B and N orbitals with the Se orbitals. The position of BN valence-band maximum is about 0.25 eV below the Fermi level for both cases similarly in the symmetric capping both TI surfaces with B on the Se, since B is placed on Se on one side of TI in both asymmetric cappings. The bulk band-gap sizes are 0.268 and 0.257 eV for "B on the top of Se atom on one side and vacuum on the other side" and "B on the top of Se on one side and N on the top of Se on the other side," respectively.

For Si-terminated SiO_2, both without and with dangling-bond passivations, show the protected Dirac cone surface state [Figs. 9(a) and 9(b)], consistent with the DOS plots in Figs. 10(a) and 10(b). Si orbitals do not mix with Se orbitals in the energy range close to the Dirac point. The band structure of only Si-terminated quartz slab without the passivation [inset of Fig. 9(a)] and its DOS plot [left inset of Fig. 10(a)] show the Si dangling-bond states within the bulk quartz band gap. These dangling-bond states are also observed around the energy level of -0.26 meV in the band structure of Si-terminated quartz with Bi_2Se_3 [Fig. 9(a)], which is confirmed by the peak value of DOS from Si orbitals at -0.26 eV in Fig. 10(a). By the hydrogen passivation, dangling-bond states are removed in the band gap of only Si-terminated SiO_2 slabs, as seen in the inset of Fig. 9(b) and the left inset of Fig. 10(b). As a result, we cannot find the SiO_2 states in the energy range of $-1 \sim 1$ eV in Figs. 9(b) and 10(b).

Figure 11(a) is the band structure of the TI surface in the presence of oxygen-terminated quartz without passivation. The DOS plot [Fig. 11(b)] shows that oxygen orbitals lie close to the Se orbitals and dominate the region around the Fermi

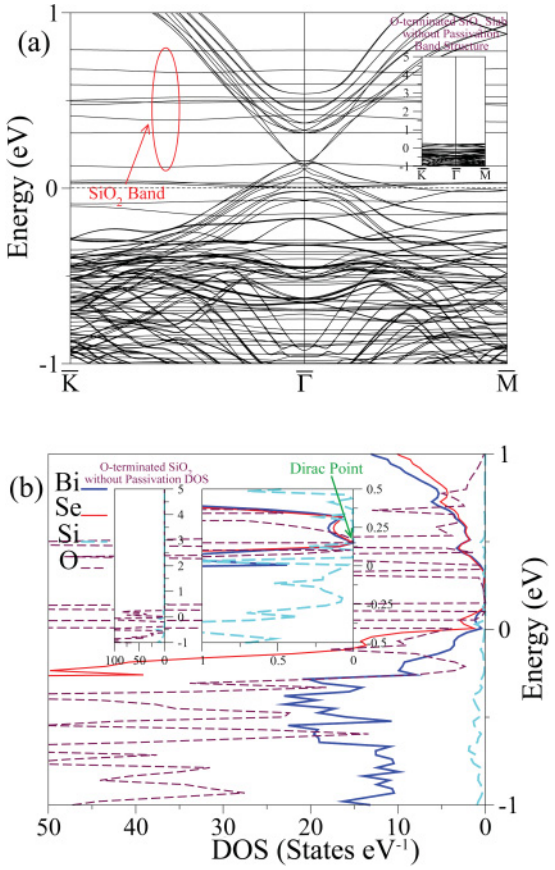

FIG. 11. (Color online) (a) Band structure of Bi_2Se_3 with oxygen-terminated quartz supercell without atomic relaxation along high-symmetry directions in the hexagonal BZ suggesting that Dirac cone is significantly affected and (b) corresponding atom-projected DOS. The strong hybridization of Se and oxygen orbitals near the Fermi level is observed. Band structure of only oxygen-terminated SiO_2 slab without passivation is in the inset of (a), and the corresponding atom-projected DOS plot is shown in the left inset of (b). The Fermi level is below the valence-band edge formed by oxygen orbitals. The Dirac point is marked with the arrow on the right inset of (b).

level. By the effect of oxygen orbitals, the Dirac cone feature is significantly distorted. However, the Dirac point still remains intact, which can be confirmed by the linear increase of Bi and Se DOS around 0.15 eV in the right inset of Fig. 11(b). It exists close to the Fermi level and is buried inside SiO_2 valence-band continuum, as shown in Figs. 11(a) and 11(b). In the band structure of only oxygen-terminated quartz without hydrogen passivation, the Fermi level is under the valence-band edge in the inset of Fig. 11(a). When oxygen-terminated quartz is put on the surface of Bi_2Se_3, the Fermi levels of two materials align, thereby pushing the Dirac point under the quartz valence band. Recent experimental studies of environmental effects on TI surface suggest the charge doping due to the presence of oxygen,[14] but argue on the insensitiveness of a TI Dirac cone. With oxygen surface passivation with atomic hydrogen, we recover a clear Dirac cone with the degeneracy point at the Fermi level [Fig. 12(a)] which is consistent with the DOS plots in Fig. 12(b). In the only oxygen-terminated quartz slab with passivation, we can observe that the Fermi level resides inside the band gap from the band structure and DOS plot

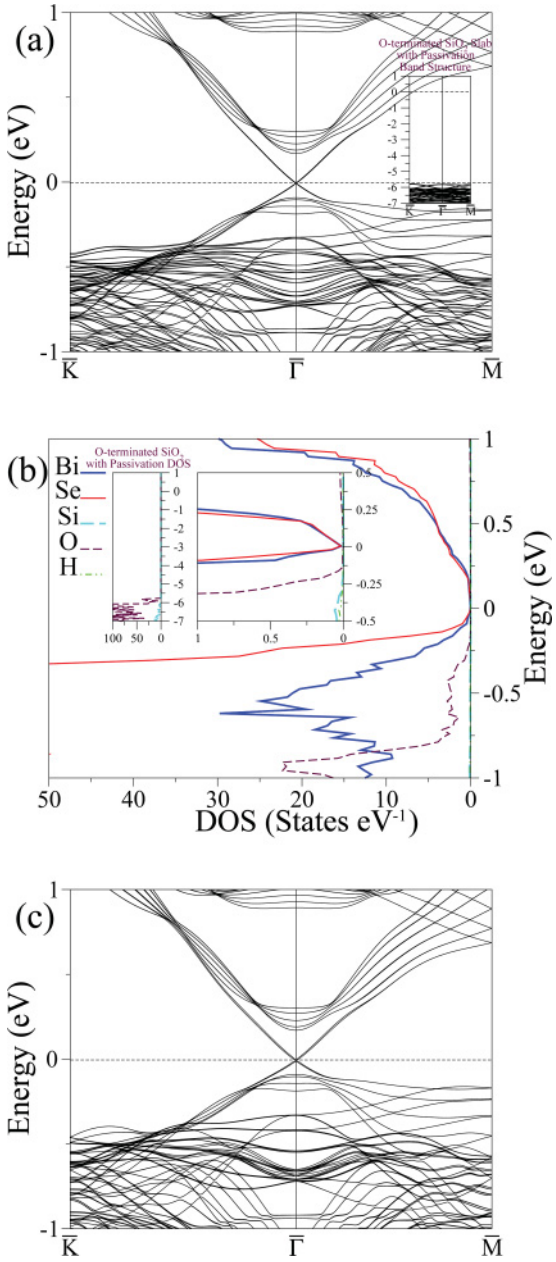

FIG. 12. (Color online) Same as Fig. 11 but now with hydrogen coverage of oxygen-dangling orbitals (a) band structure without atomic relaxation and (b) corresponding atom-projected DOS. The Dirac cone of TI is recovered due to noninteraction of Se and oxygen orbitals. (c) Same case with atomic relaxation. The Dirac cone feature is not affected by the atomic relaxation. Band structure of only oxygen-terminated SiO_2 slab with passivation is in the inset of (a), and the corresponding atomic-projected DOS plot is shown in the left inset of (b). The Fermi level is inside the gap.

shown in the inset of Fig. 12(a) and the left inset of Fig. 12(b), respectively. Therefore, the Fermi-level matching between quartz and Bi_2Se_3 occurs without pulling down the Dirac cone surface states into the quartz valence band. Atomic relaxations of interfacial atoms has no effect on the Dirac cone as well as its degeneracy [Fig. 12(c)]. For all SiO_2 cappings, except oxygen-terminated quartz without passivation, the Dirac cones reside inside the bulk band gap of about 0.26 eV.

TABLE II. Hexagonal unit-cell lattice constant a of ternary TIs and strains on dielectrics by the lattice mismatch at the interface.

TI	a (nm)	Strain on SiO_2	Strain on BN
Bi_2Se_2Te	0.422	0.83% compressive	0.23% compressive
Bi_2Te_2Se	0.428	0.57% tensile	0.92% compressive

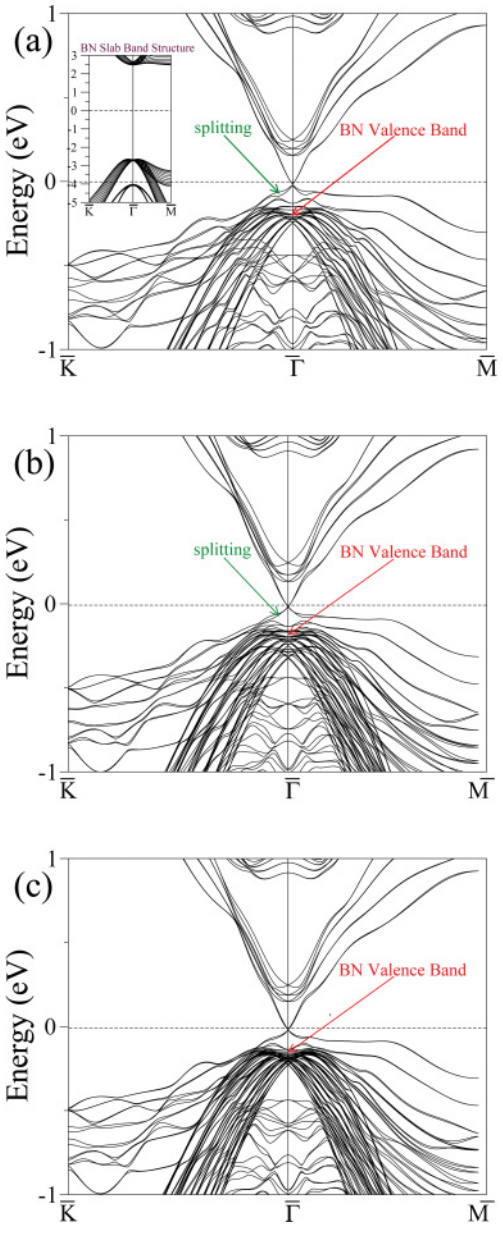

FIG. 13. (Color online) Band structure of Bi_2Se_2Te/BN supercell along high-symmetry directions of the hexagonal BZ for asymmetric capping cases (a) B on the top of Se on one side and vacuum on the other side of TI film and (b) B on the top of the Se atom on one side and N on the top of the Se atom on the other side, and for the symmetric capping case (c) B on the top of Se on both sides of TI film. The atomic relaxation is not considered. The Dirac cone and its degeneracy at the $\bar{\Gamma}$ point are not disturbed in the presence of crystalline BN thin film. The position of the BN valence-band edge can be estimated by the band structure of the BN slab without TI in the inset of (a).

B. Thin films of ternary TIs Bi_2Se_2Te and Bi_2Te_2Se

In this section, we address the dielectric effects on the electronic structure of ternary TIs of Bi and chalcogen.

1. Construction of supercell structure

The construction of interface structures for ternary TI Bi_2Se_2Te (Bi_2Te_2Se) is similar with that for Bi_2Se_3, except the thickness of TI films. Since 4 QLs is predicted as a minimum thickness to preserve the Dirac cone band structure for ternary TIs,[19] 4-QL-thick TI films are used in the ternary TI calculations instead of 6 QLs in the interface structure of binary TI Bi_2Se_3 with dielectrics.

For the BN dielectric capping, the BN of the $3d_{\text{B-N}} \times 3d_{\text{B-N}}$ lattice structure is matched in-plane with the 1×1 Bi_2Se_2Te (Bi_2Te_2Se) cell. Since we keep the lattice constant of Bi_2Se_2Te (Bi_2Te_2Se) and fit BN into it, BN is under about 0.23% compressive strain (0.92% compressive strain) in Table II. Six layers of BN (∼1.7 nm) is put on each side of 4 QLs Bi_2Se_2Te (Bi_2Te_2Se). For the SiO_2 dielectric, the 1×1 SiO_2 cell is fit with the 2×2 Bi_2Se_2Te (Bi_2Te_2Se) cell in-plane, which results in 0.83% compressive strain (0.57% tensile strain) on SiO_2, as summarized in Table II. Two unit cells of SiO_2 are stacked on both sides of 4 QLs Bi_2Se_2Te (Bi_2Te_2Se) in the z direction.

Four configurations of Se (Te) positions on the TI surfaces with respect to B and N positions on the BN layer were investigated and found to be energetically quite similar, the same as our studies on the binary TI with BN. The optimal distance between BN and Bi_2Se_2Te (Bi_2Te_2Se), minimizing the total energy, is found to be 0.32 nm (0.3 nm). We considered asymmetric capping, B on the top of Se (Te) on one side and vacuum on the other side or B on the top of Se (Te) on one side and N on the top of Se (Te) on the other side, as well as symmetric capping, B on the top of Se (Te) on both sides. For the SiO_2 capping, we focused on the oxygen-terminated SiO_2 on both sides of TI without saturating oxygen dangling-bond states as a critical case because there are reports, as discussed in the previous section, that oxygen dangling-bond states may play a crucial role in modifying TI surface. Only Bi_2Te_2Se with oxygen-terminated quartz was studied because we know that Se orbitals lie close in energy with the oxygen orbitals from the previous study of Bi_2Se_3 and the ternary TI Bi_2Se_2Te is structurally similar to the binary TI Bi_2Se_3 regarding the atom species Se of top and bottom surfaces. Atomic relaxation was not considered for ternary TIs because the rearrangement of atomic positions was found to have no substantial effect in the binary TI with dielectrics.

2. Results and discussion

Computed band structures of the Bi_2Se_2Te/BN supercell are seen in Fig. 13. Both asymmetric capping, in Figs. 13(a) (B on the top of Se on one side and vacuum on the other side) and 13(b) (B on the top of Se on one side and N on the top of Se on the other side), and symmetric capping in Fig. 13(c) (B on the top of Se on both sides) indicate that the Dirac point and the surface-state dispersion are preserved. However, small splitting between top and bottom surface bands occurs in the asymmetric case, which is induced by different environments on opposite surfaces, while no such splitting exists in the symmetric structure. The valence-band maximum is about 0.25 eV below for all three cases as we can estimate

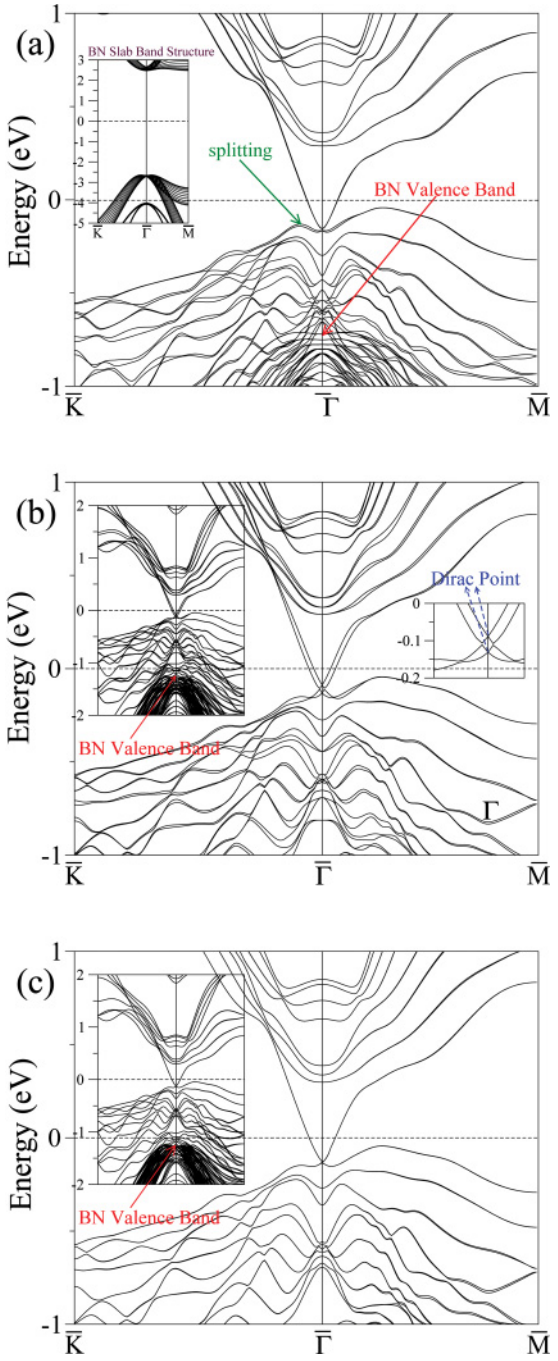

FIG. 14. (Color online) Band structure of the Bi_2Te_2Se/BN supercell along high-symmetry directions of the hexagonal BZ for asymmetric capping cases (a) B on the top of Te on one side and vacuum on the other side of TI film and (b) B on the top of the Te atom on one side and N on the top of the Te atom on the other side, and for the symmetric capping case (c) B on the top of Te on both sides of the TI film. The atomic relaxation is not considered. The Dirac cone at the $\bar{\Gamma}$ point is not disturbed in the presence of crystalline BN thin film. The fourfold degeneracy is lifted to two twofold degeneracies at the $\bar{\Gamma}$ point in the inset of (b). The position of the BN valence-band maximum can be found by the band structure of the BN slab without TI in the inset of (a).

from the band structure of only BN slab in the inset of Fig. 13(a) and atom-projected DOS plots (figures not shown). The bulk band-gap sizes (around 0.251 eV) in all BN cappings for Bi_2Se_2Te increase a little bit as compared with the bulk gap (0.204 eV) of only 4 QLs Bi_2Se_2Te.

Figure 14 shows band structures of the Bi_2Te_2Se/BN supercell. In Fig. 14(a), the asymmetric capping of B on the top of Te on one side and vacuum on the other side, the fourfold degeneracy at the Dirac point is maintained, but two opposite surface bands seem to split. Another asymmetric capping that Te is on the top of B on one side and N on the other side leads to the split of fourfold degeneracy into two twofold degeneracies at the $\bar{\Gamma}$ point. The twofold degeneracy on each surface band still remains due to Kramer's theorem which requires that the twofold degeneracy at the time-reversal invariant momenta points is protected in the absence of time-reversal symmetry-breaking perturbations. On the other hand, in the symmetric structure of B on the top of Te on both sides, surface bands on both sides are perfectly aligned, as seen in Fig. 14(c). In BN cappings of Bi_2Te_2Se, the bulk band-gap sizes (around 0.33 eV) are a bit larger than 0.325 eV, the bulk band gap of 4 QLs Bi_2Te_2Se without BN.

For the capping Bi_2Te_2Se with the oxygen-terminated quartz without dangling-bond passivation, the Dirac cone

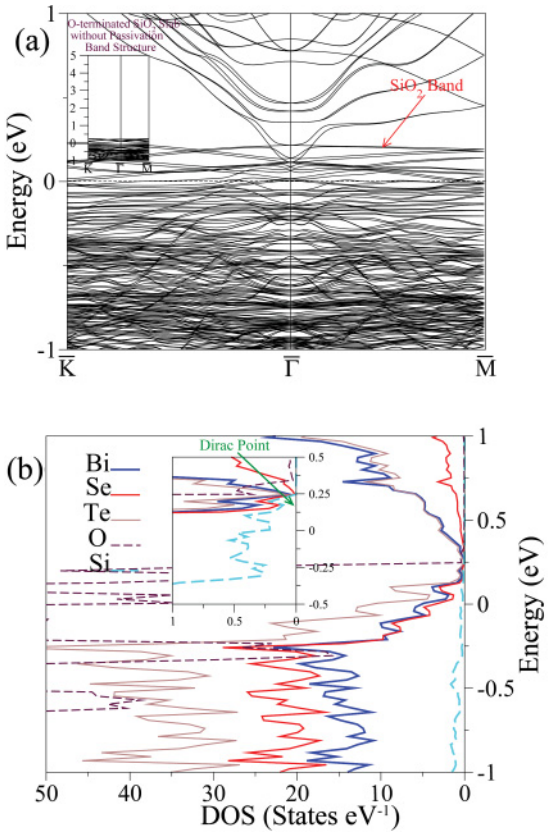

FIG. 15. (Color online) (a) Band structure of Bi_2Te_2Se with oxygen-terminated quartz supercell without atomic relaxation along high-symmetry directions in the hexagnoal BZ suggesting that Dirac cone is affected and (b) corresponding atom-projected DOS. The Dirac point of TI is buried into quartz valence bands. The band structure of only oxygen-terminated SiO_2 slab without passivation is in the inset of (a). The Fermi level is below the valence-band edge formed by oxygen orbitals. The Dirac point is marked with an arrow in the inset of (b).

surface states are highly influenced by the oxygen dangling-bond states in Fig. 15(a). From the DOS plot in Fig. 15(b), Bi, Te, and Se orbitals are overlapped with oxygen orbitals near the Dirac point. The Dirac point indicated in the inset of Fig. 15(b) is within the valence bands of quartz. The DOS values for Bi, Se, and Te at the Dirac point are not zero as shown in the inset because the Dirac point is already buried under the bulk valence-band maximum of Bi_2Te_2Se.[19] Similarly with Bi_2Se_3, oxygen dangling states modify Dirac cone surface states without breaking the Dirac point.

IV. SUMMARY AND CONCLUSIONS

We use a density-functional-based electronic structure method and atom-projected DOS to study the perturbations from dielectric cappings to the Dirac cone surface states of Bi-based binary and ternary TIs. Two crystalline dielectrics BN and quartz were considered with both symmetric and asymmetric cappings. Our study suggests that oxygen coverage substantially affects the Dirac cone, consistent with a recent experimental study. All other surface dielectric terminations have no significant effect on the TI surface states.

ACKNOWLEDGMENTS

The authors acknowledge financial support from the Nanoelectronics Research Initiative supported Southwest Academy of Nanoelectronics (NRI-SWAN) Center. We thank Texas Advanced Computing Center (TACC) for computational support (TG-DMR080016N).

*jiwon.chang@utexas.edu

[1] X.-L. Qi and S.-C. Zhang, Phys. Today **63**(1), 33 (2010).
[2] M. Z. Hasan and C. L. Kane, Rev. Mod. Phys. **82**, 3045 (2010).
[3] B. Yan, H.-J. Zhang, C.-X. Liu, X.-L. Qi, T. Frauenheim, and S.-C. Zhang, Phys. Rev. B **82**, 161108 (2010).
[4] D. Xiao, Y. Yao, W. Feng, J. Wen, W. Zhu, X. Q. Chen, G. M. Stocks, and Z. Zhang, Phys. Rev. Lett. **105**, 096404 (2010).
[5] W. Feng, D. Xiao, J. Ding, and Y. Yao, Phys. Rev. Lett. **106**, 016402 (2011).
[6] S. Chadov, X.-L. Qi, J. Kbler, G. H. Fecher, C. Felser, and S.-C. Zhang, Nat. Mater. **9**, 541 (2010).
[7] H. Lin, L. A. Wray, Y. Xia, S. Xu, S. Jia, R. J. Cava, A. Bansil, and M. Z. Hasan, Nat. Mater. **9**, 546 (2010).
[8] H. Zhang, C.-X. Liu, X.-L. Qi, X. Dai, Z. Fang, and S.-C. Zhang, Nat. Phys. **5**, 438 (2009).
[9] A. A. Burkov and D. G. Hawthorn, Phys. Rev. Lett. **105**, 066802 (2010).
[10] Y. S. Hor, P. Roushan, H. Beidenkopf, J. Seo, D. Qu, J. G. Checkelsky, L. A. Wray, D. Hsieh, Y. Xia, S.-Y. Xu, D. Qian, M. Z. Hasan, N. P. Ong, A. Yazdani, and R. J. Cava, Phys. Rev. B **81**, 195203 (2010).
[11] J. P. Perdew, K. Burke, and M. Ernzerhof, Phys. Rev. Lett. **77**, 3865 (1996).
[12] C. R. Dean, A. F. Young, I. Meric, C. Lee, L. Wang, S. Sorgenfrei, K. Watanabe, T. Taniguchi, P. Kim, K. L. Shepard, and J. Hone, Nat. Nanotech. **5**, 722 (2010).
[13] J. Xue, J. Sanchez-Yamagishi, D. Bulmash, P. Jacquod, A. Deshpande, K. Watanabe, T. Taniguchi, P. Jarillo-Herrero, and B. J. LeRoy, Nat. Mater. **10**, 282 (2010).
[14] D. Kong, J. J. Cha, K. Lai, H. Peng, J. G. Analytis, S. Meister, Y. Chen, H-J. Zhang, I. R. Fisher, Z-X. Shen, and Y. Cui, ACS Nano **5**, 4698 (2011).
[15] T. Ozaki and H. Kino, Phys. Rev. B **72**, 045121 (2005).
[16] T. Ozaki, Phys. Rev. B **67**, 155108 (2003).
[17] C.-X. Liu, X.-L. Qi, H. J. Zhang, X. Dai, Z. Fang, and S.-C. Zhang, Phys. Rev. B **82**, 045122 (2010).
[18] Y. Zhang, K. He, C.-Z. Chang, C.-L. Song, L.-L. Wang, X. Chen, J.-F. Jia, Z. Fang, X. Dai, W.-Y. Shan, S.-Q. Shen, Q. Niu, X.-L. Qi, S.-C. Zhang, X. -C. Ma, and Q.-K. Xue, Nat. Phys. **6**, 584 (2010).
[19] J. Chang, L. F. Register, S. K. Banerjee, and B. Sahu, Phys. Rev. B **83**, 235108 (2011).
[20] See [http://cst-www.nrl.navy.mil/lattice/struk/b_k.html].
[21] K. Watanabe, T. Taniguchi, and H. Kanda, Nat. Mater. **3**, 404 (2004).
[22] See [http://cst-www.nrl.navy.mil/lattice/struk/sio2a.html].
[23] E. P. O'Reilly and J. Robertson, Phys. Rev. B **27**, 3780 (1983).